ACS APPLIED MATERIALS & INTERFACES

Research Article

Cite This: ACS Appl. Mater. Interfaces XXXX, XXX, XXX−XXX

www.acsami.org

Perceiving Linear-Velocity by Multiphoton Upconversion

Hai Huang,[†,§,∥] Feng Huang,[*,†,§,∥] Lin Lin,[†,§,∥] Zhuohong Feng,[†,§,∥] Yao Cheng,[‡] Yuansheng Wang,[‡] and Daqin Chen[*,†,§,∥]

[†]College of Physics and Energy, Fujian Normal University, Fujian Provincial Key Laboratory of Quantum Manipulation and New Energy Materials, Fuzhou 350117, China

[‡]CAS Key Laboratory of Design and Assembly of Functional Nanostructures, Fujian Institute of Research on the Structure of Matter, Chinese Academy of Sciences, Fuzhou, Fujian 350002, China

[§]Fujian Provincial Engineering Technology Research Center of Solar Energy Conversion and Energy Storage, Fuzhou 350117, China

[∥]Fujian Provincial Collaborative Innovation Center for Optoelectronic Semiconductors and Efficient Devices, Xiamen 361005, China

Supporting Information

ABSTRACT: Up to now, the rising edge of the upconversion process does not receive due attention. Herein, a demonstration utilizing the feature of the rising edge to practically detect the linear-velocity of an object is presented. Typically, upconversion processes with different numbers of participant photons would exhibit diversity in the rising edge. On this account, when the emitter is moving, the emission intensity ratio of different multiphoton processes will vary with changing linear-velocity, which enables accurate speed detection through spectral analysis. To illustrate this principle, in this work, the modeling and numerical simulation were first performed, and then experimental demonstration was carried out in which core−shell upconversion nanocrystals were elaborately designed and fabricated as the speed sensing probe to calibrate the speed of a homemade turnplate. It is believed that the present work will exploit a novel speed sensing method and find a new application for lanthanide-doped upconversion materials.

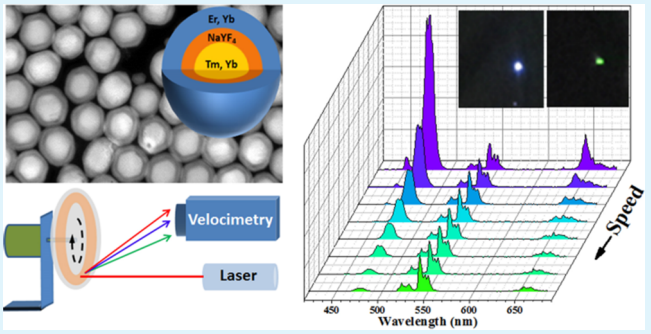

KEYWORDS: *Upconversion, Non-steady-state emission, Velocimetry, Fluoride nanocrystals, Lanthanide luminescent materials*

In the past decades, lanthanide-doped luminescent materials have played a very active role in sensing applications, such as biosensing (immunological detection,[1−3] cell imaging,[4,5] in vivo labeling,[6−8] and so on) as well as environment sensing (thermometry,[9−11] particular ion/molecular detection,[12,13] and so on). All of these applications mainly concern two sections of the luminescence behaviors, that is, steady-state emission and time-resolved decay.[14−20] As for the rising edge of the emission process, less attention has been paid to, let alone developing critical application, although it is also an important section of the luminescence behavior.

Actually, the optical response, especially the temporal response of the upconversion (UC) phosphors, is highly related to the rising edge, which is manipulatable by the component and host-structure.[21,22] Very recently, attention has been paid to this issue. For example, Xia et al. made use of the long rising time and long lifetime of Mn^{2+} ions in $RbCaF_3$ to achieve dynamic color separation and develop its application in multiple anticounterfeiting.[23] However, up to now, many regions of this field still remain to be exploited, especially for developing some crucial sensing technologies. Well in this work, we will make a demonstration of a potential application, which utilizes the feature of the rising edge and thus the temporal response of UC phosphor to detect the linear-velocity of the object. The present work will provide a new sensing technology and find a novel application for lanthanide luminescent materials. Compared to conventional optical speed sensing methods, such as reflection counting, Doppler velocimetry, or camera-based image velocimetry,[24−26] the present speed sensing method exhibits potential advantages of remote-type detection, high sensitivity, and high spatial resolution. The following results would indicate broad potential applications for the proposed velocimetric strategy in the fields of vehicle monitoring to blood flow velocity labeling.

For a clear illumination on the proposed speed sensing principle, first of all, we established an idealized ladder-like multi-energy-level model to illustrate the non-steady-state feature of the UC process, as illustrated in Figure 1a. Based on the model, the changing rates of the populations (dN/dt) and

Received: September 26, 2019
Accepted: November 14, 2019
Published: November 14, 2019

DOI: 10.1021/acsami.9b17507
ACS Appl. Mater. Interfaces XXXX, XXX, XXX−XXX

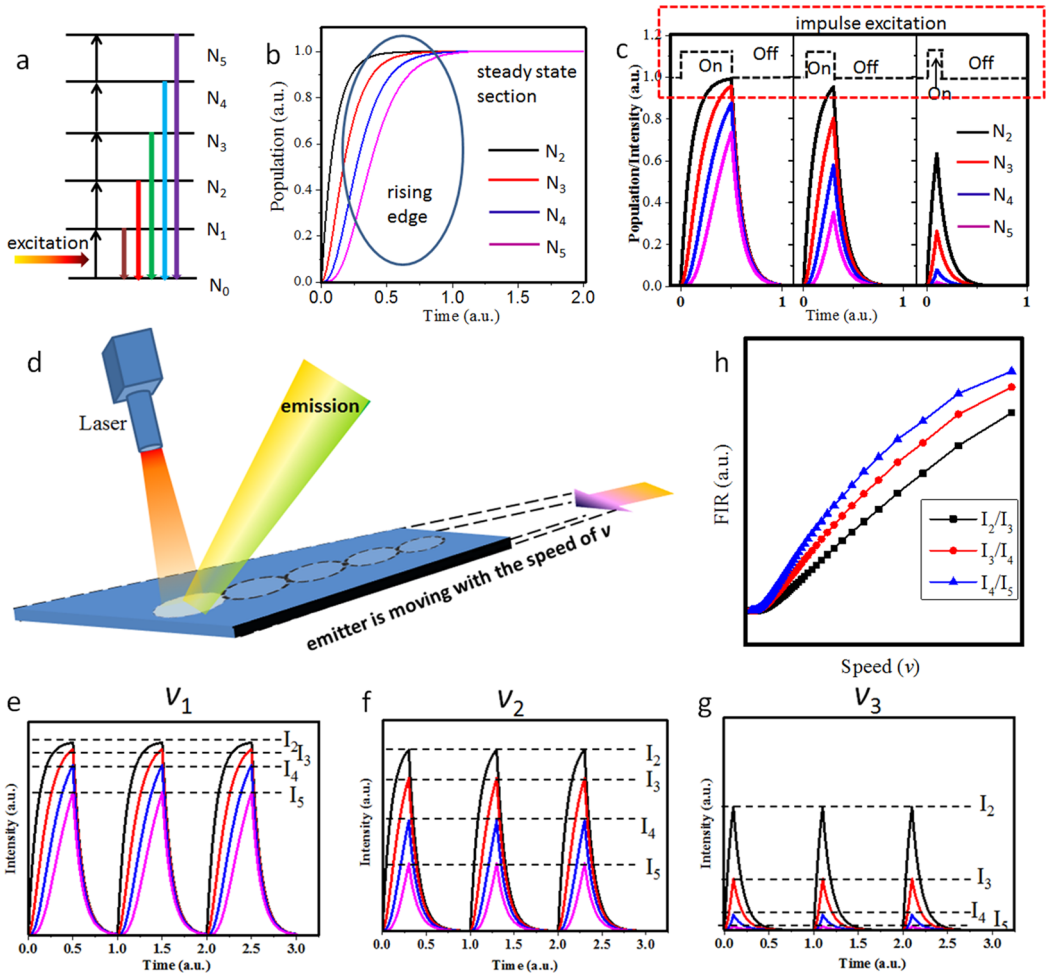

Figure 1. (a) Schematic diagram of an ideal ladder-like multi-energy-level model. (b) Calculated curves of populations versus time on various energy levels when steady-state excitation is applied. (c) Calculated population and thus the temporal luminescence intensity versus time on every energy level when pulse excitations with different widths are applied. (d) Schematic showing excitation and emission of a moving phosphor. (e–g) Simulated time-related luminescence behaviors of different UC processes, assuming that the phosphor is moving with three specific speeds (v_1, v_2, and v_3, $v_1 < v_2 < v_3$). (h) Calculated fluorescence intensity ratios of different UC processes versus moving speed.

the temporal luminescent intensities are related to laser pumping power density, absorption cross sections, and radiative transition rates. Herein, to simplify the calculation, we ignore the nonradiative and cross-relaxation processes and only consider the radiative transition from excited states to the ground state; therefore, the rate equations can be written as follows

$$\frac{d}{dt}\begin{pmatrix} N_0 \\ N_1 \\ N_2 \\ N_3 \\ \vdots \end{pmatrix} = \begin{pmatrix} -wc_0 & A_1 & A_2 & A_3 & \cdots \\ wc_0 & -wc_1 - A_1 & 0 & 0 & \cdots \\ 0 & wc_1 & -wc_2 - A_2 & 0 & \cdots \\ 0 & 0 & wc_2 & -wc_3 - A_3 & \cdots \\ \cdots & \cdots & \cdots & \cdots & \cdots \end{pmatrix} \begin{pmatrix} N_0 \\ N_1 \\ N_2 \\ N_3 \\ \vdots \end{pmatrix} \quad (1)$$

where w is the power of the excitation, A_1, A_2, A_3., are the radiative transition rates of corresponding energy levels (herein, this parameter specifically refers to the radiative transition rates from the corresponding excited state to the ground state, ignoring the transition from one excited state to another excited state), and c_0, c_1, c_2., are the absorption cross section of each level.

The analytical solutions are expressed in Section S1. Through numeric iteration, the population on each level can be calculated, which is displayed in Figure 1b. Obviously, in the rising edge section, the slope of the rising curve relates to the number of photons required for pumping to the corresponding level. This result indicates that, when pulse excitation is applied, the temporal luminescence intensities from different levels will exhibit diversity (Figure 1c). Moreover, with the reduction of laser pulse width, the diversity becomes more and more severe.

Assuming a scene that a UC sample is moving while the excitation light (the size of the beam spot is d) is motionless, as schematically illustrated in Figure 1d, the sample can be counted as several emitting units with the size of d. Each unit is excited only when it passes through the region of the excitation beam spot and, therefore, can be seen only when receiving pulsing excitation (pulse width $\tau = d/v$, where v is the linear-velocity of the emitter). In such a case, the overall luminescence can be

DOI: 10.1021/acsami.9b17507
ACS Appl. Mater. Interfaces XXXX, XXX, XXX−XXX

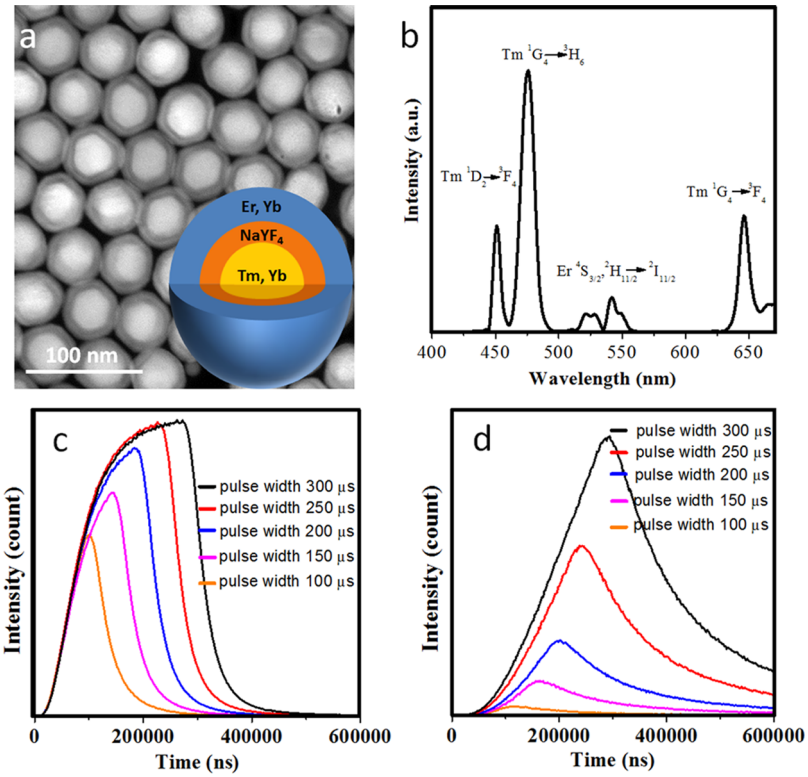

Figure 2. (a) High-angle annular dark-field scanning transmission electron microscope (HAADF-STEM) image of the synthesized Tm/Yb:$NaGdF_4$@$NaYF_4$@Er/Yb:$NaGdF_4$ UCNCs; the inset is the schematic core−shell−shell configuration. (b) UC emission spectrum of core−shell−shell UCNCs, excited with a steady-state 980 nm laser. Time-dependent emitting intensities from (c) Er^{3+} (543 nm) and (d) Tm^{3+} (475 nm) ions when different pulse widths are applied.

approximated to be the accumulation of sequenced temporal emissions from each sample unit, as displayed in Figure 1e−g. Undoubtedly, with the increase of the moving speed, the pulse width inflicted on each unit would reduce, which promotes the diversity of luminescence intensity from different levels (Figure 1e−g). Consequently, the fluorescence intensity ratio (FIR) of different levels would exhibit remarkable dependence on the linear-velocity. Figure 1h displays the simulated FIRs (I_2/I_3, I_3/I_4, and I_4/I_5), all of which exhibit a monotone rise with the increase of velocity. The "higher-order" FIRs (e.g., I_2/I_4, I_3/I_5, and I_2/I_5) are presented in Figure S1, which also exhibit similar monotone variation but severe dependence on velocity. Higher-order FIRs are undoubtedly more sensitive to the velocity since the more photons participate in the upconversion process, the longer the rising edge would exhibit, and thus, more severe diversity in luminescence intensity would appear. These results indicate the potential of a spectral velocimetry technique that employs a UC material as the probe.

It is worthy to note that the above calculation is idealized, which only simulates the excited-state absorption , while for practical use, for brightening the luminescence, the sensitizing ions are always introduced, which makes the energy transfer upconversion (ETU) become dominated. The ETU process might prolong the rising edge for each level relatively,[22] but the diversity still remains. To ensure this and confirm the feasibility of this proposed speed sensing strategy, in the present work, core−shell UC nanocrystals (UCNCs) composed of $NaYF_4$/$NaGdF_4$ are chosen as the host, which is doped with Tm, Er, and Yb activators to act as the typical probing materials. Concretely, we constructed the Tm/Yb:$NaGdF_4$@$NaYF_4$@Er/Yb:$NaGdF_4$ NCs, as shown in Figure 2a (the concentrations of Tm and Yb in the core are 3 and 37%, respectively, while those of Er and Yb in the outer shell are 1 and 39%, respectively). In this nano-architecture, Er dopants in the shell are responsible for providing the two-photon emission, Tm activators in the core take charge for exhibiting high-ordered UC (i.e., three-photon and four-photon UC), and the middle $NaYF_4$ inert-shell plays a role of spatial isolation between Tm and Er. Herein, we adopt such a configuration intending to obtain initially a relatively more intense Tm^{3+} ion luminescence than Er^{3+} ions since high-ordered UC would suffer a more severe attenuation with the increase of the moving speed when we perform the velocimetry experiment, while the middle $NaYF_4$ layer can not only eliminate the $Tm^{3+} \rightarrow Er^{3+}$ energy transfer trough the interface but also isolate the $Tm^{3+} \rightarrow Gd^{3+} \rightarrow Er^{3+}$ energy migration from the core to the shell. X-ray diffraction (XRD) patterns (Figure S2) identify that all the synthesized NCs are hexagonal-phase $NaYF_4$/$NaGdF_4$. The detailed microstructure observations for these core−shell UCNCs are presented in Figure S3.

The steady-state UC spectrum of the synthesized core−shell NCs is presented in Figure 2b. The four-photon UC ($Tm\ ^1D_2 \rightarrow\ ^3F_4$ at 450 nm), three-photon UC ($Tm\ ^1G_4 \rightarrow\ ^3H_6$ at 475 nm, and $^1G_4 \rightarrow\ ^3F_4$ at 648 nm) as well as the two-photon UC ($Er\ ^4S_{3/2}$, $^2H_{11/2} \rightarrow\ ^4I_{15/2}$ at 543 nm) emissions can be well discerned. Impulse excitations with different pulse widths are applied to illustrate the diverse temporal response of the two-photon Er UC and three-photon Tm UC. As shown in Figure 2c,d, with the decrease of the pulse width, both Er and Tm emissions exhibit a decline at the maximal intensity, but obviously the 475 nm three-photon emission exhibits a more severe decline than the 543 nm two-photon emission. This experimental result agrees well with the above discussion based

DOI: 10.1021/acsami.9b17507
ACS Appl. Mater. Interfaces XXXX, XXX, XXX−XXX

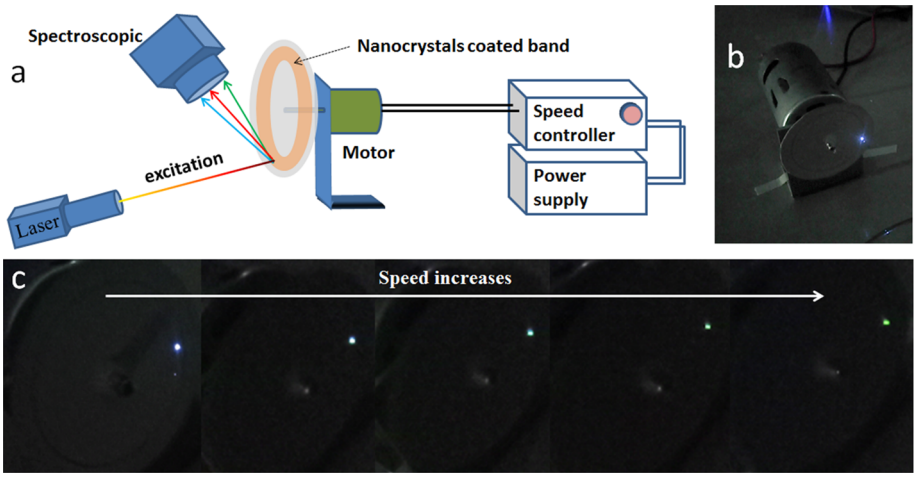

Figure 3. (a) Configuration of speed sensing equipment. (b) Photo of the motionless turnplate coated with Tm/Yb:$NaGdF_4$@$NaYF_4$@Er/Yb:$NaGdF_4$ UCNCs, under excitation of a 980 nm laser (50 mW/mm^2). (c) Photos of the rotating turnplate with increasing speed, under excitation of a 980 nm laser.

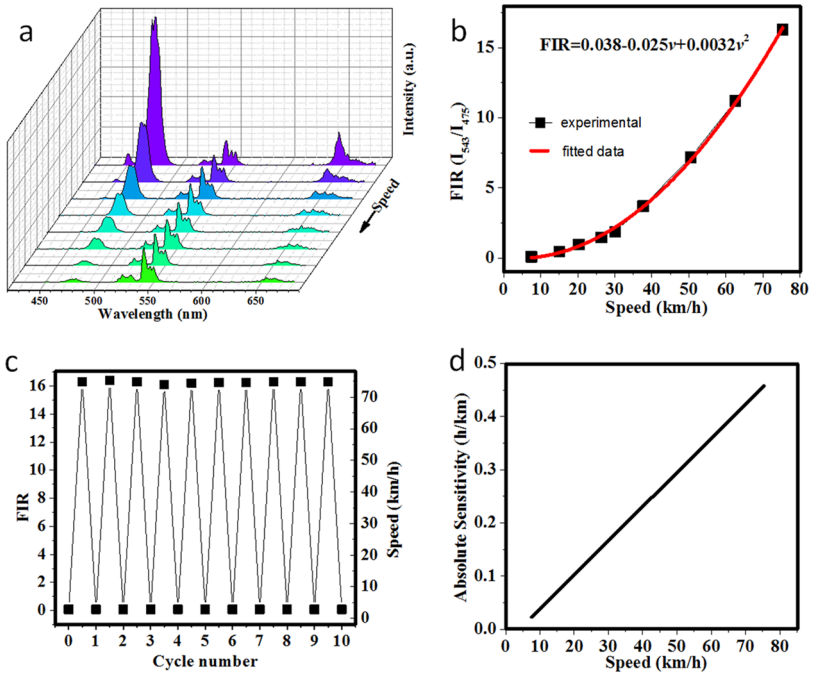

Figure 4. (a) Speed-dependent UC emission spectra of Tm/Yb:$NaGdF_4$@$NaYF_4$@Er/Yb:$NaGdF_4$ NCs. (b) Plot of FIR versus speed fitted with a quadratic polynomial. (c) FIR at a motionless state and at a speed of 75 km/h for accelerating and decelerating cycles. (d) Calculated sensitivity versus speed.

on numerical simulation, indicating the feasibility for performing speed sensing via employing the FIR of 543 nm emission to a 475 nm one.

Furthermore, a demonstration of speed sensing was performed. The core−shell UCNCs were coated on a rounded board, which is fixed on a motor to enable the rotation (Figure 3a,b). This device was then equipped in the sample chamber of a spectrofluorimeter (Figure S4). With the increase of the rotation rate and thus the linear speed of the sample, the emission color gradually changes from blue to green (Figure 3c). Movie S1 shows this chromatic phenomenon during the acceleration and deceleration of the turnplate. This is ascribed to the alteration of Er and Tm emission, as exhibited in Figure 4a. The FIR (I_{543}/I_{475}) value versus speed exhibits a remarkable monotone variation (Figure 4b). Therefore, this FIR parameter can be employed as the speed sensing index. Figure 4c presents the measured FIRs at a speed of 7.5 km/h (0.087 ± 0.001) and at a speed of 75 km/h (16.3 ± 0.02) for 10 times accelerating and decelerating cycles, which indicates the stability of this speed sensing method. To calculate speed sensitivity ($S = dFIR/dv$, the unit of S is $(km/h)^{-1}$, and herein, we simplify it as h/km), we adopt Taylor expansion to express the relationship of FIR versus speed, regarding FIR as a polynomial function of velocity (see Section S1). As exhibited in Figure 4b, the experimental data match well with a quadratic polynomial. Accordingly, the speed sensitivity can be evaluated, as presented in Figure 4d. Notably, as the speed increases from 7.5 to 75 km/h, the S value rises up from 0.023 to 0.45 h/km. This phenomenon is reasonable because, when the moving speed of the emitter is low, both the two-photon and three-photon UC emissions are still approx-

DOI: 10.1021/acsami.9b17507
ACS Appl. Mater. Interfaces XXXX, XXX, XXX−XXX

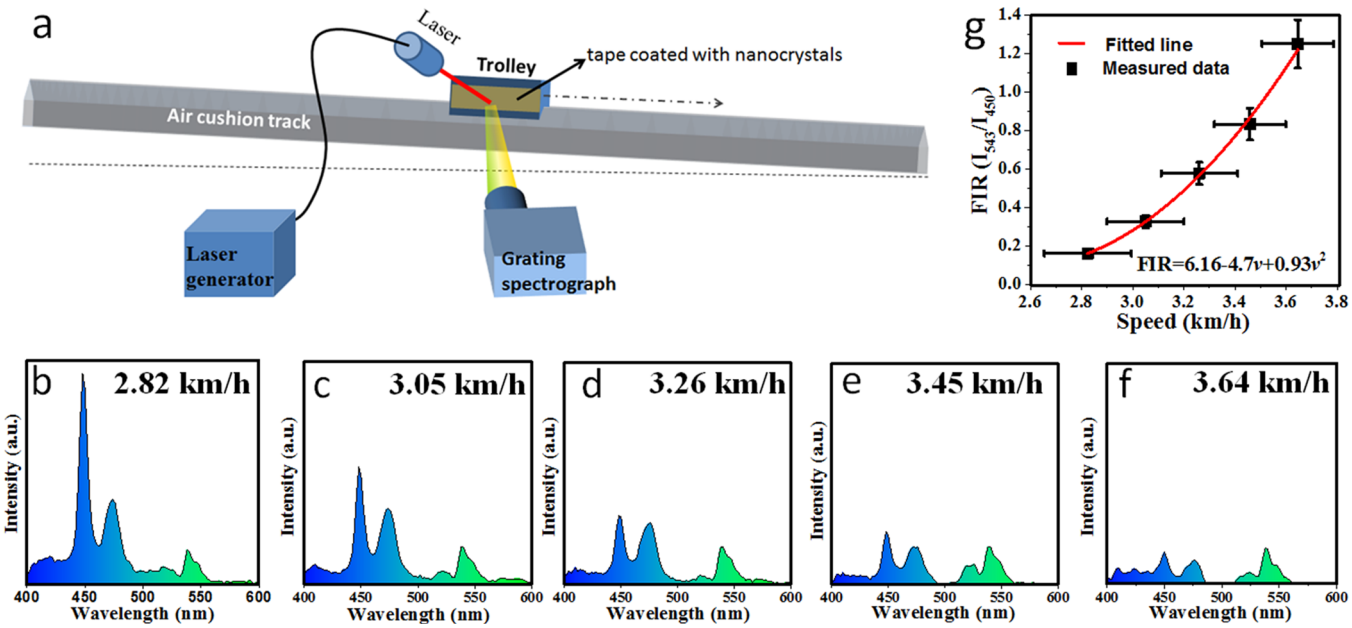

Figure 5. (a) Schematic illustration of experimental setup for simulating velocimetry for an object with rectilinear motion. (b–f) The captured temporal emission spectra for a trolley moving at various speeds; all the spectra are normalized to the emission peak at 543 nm. (g) Plot of FIR (I_{543}/I_{450}) versus speed fitted with quadratic polynomial. The x error bars come from taking the length of the trolley into account, and the y error bars originate from the background noise of the CCD grating spectrograph (ΔI, Figure S8), which is determined by following the equation of $\Delta\mathrm{FIR} = \Delta I\frac{\sigma\mathrm{FIR}}{\sigma I_{450}} + \Delta I\frac{\sigma\mathrm{FIR}}{\sigma I_{543}} = \frac{\Delta I}{I_{450}}(1 + \mathrm{FIR})$.

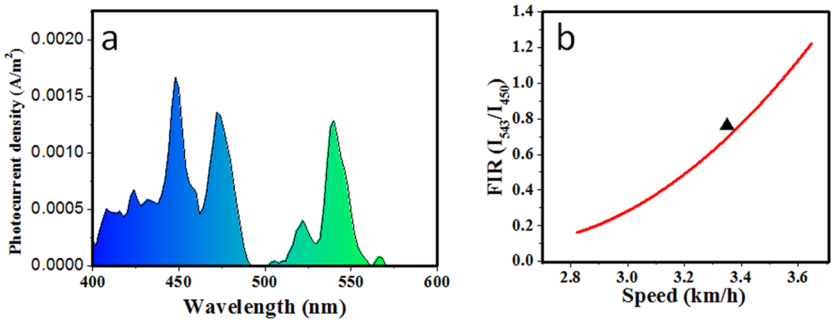

Figure 6. (a) Temporal emission spectrum of a trolley passing through the excitation spot at a speed of 3.32 km/h. (b) The measured FIR compared with the rating curve.

imate to the steady state; that is, their FIR is relatively dull to the speed changing. Fortunately, in our speed sensing system, it is easy to obtain a promoted sensitivity at a low speed. For example, we can take the four-photon process into account. Specifically, we can utilize the FIR of three-photon UC to four-photon UC (i.e., I_{475}/I_{450}) or even two-photon to four-photon UC (i.e., I_{543}/I_{450}). Figure S5 demonstrates the values of I_{475}/I_{450} and I_{543}/I_{450} versus speed, as well as the sensitivities of these two FIRs. When using FIRs of I_{475}/I_{450} and I_{543}/I_{450} as sensing indexes, remarkably higher sensitivities can be achieved (up to 0.5 and 0.7 h/km, respectively, at a speed of 7.5 km/h). Therefore, this proposed velocimetric method is expected to enable the modulation according to the target speed range, which is favorable for practical speed detection.

Finally, to illustrate the usability of the proposed velocimetry in practice application, the detection for the rectilinear moving object is simulated. We introduce a length-scaled air cushion track, which is tilted by 3° to enable the slide of a trolley on it (Figure S6). The instantaneous velocity of the trolley when it passes through the excitation spot is controlled by its initial position, and the maximal velocity of trolley is 4.5 km/h. The core–shell UCNCs were coated on the side of the trolley. To realize sensitive velocimetry at a relatively low speed by using FIR of two-photon to four-photon UC (i.e., I_{543}/I_{450}), high-content (57 mol %) Yb^{3+} ions were doped into the core to enhance four-photon UC emission assigned to the Tm $^1D_2 \rightarrow {}^3F_4$ transition (Figure S7). A CCD grating spectrograph, which is capable of capturing a whole spectrum within 500 ms, was employed to collect the emission spectra from the UCNCs, as illustrated in Figure 5a. The captured temporal emission spectra for a trolley moving at various speeds are presented in Figure 5b–f. A remarkable monotone increase of FIR (I_{543}/I_{450}) with the speed is observed (Figure 5g), from which the rating curve of FIR diverse velocity is obtained for velocimetry (red line in Figure 5g).

Based on this rating curve, practical velocimetry for the trolley can be carried out. For example, the trolley was put at a random selected position of the air cushion track, and then it started to slide. After it passed through the excitation spot, a temporal emission spectrum was captured (Figure 6a). The FIR (I_{543}/I_{450}) is read out to be 0.76, and a speed of 3.39 km/h is indexed from the rating curve. This value is close to the actual speed of

DOI: 10.1021/acsami.9b17507
ACS Appl. Mater. Interfaces XXXX, XXX, XXX–XXX

3.32 km/h, as illustrated in Figure 6b, confirming its feasibility of the proposed velocimetric strategy.

The above simulated application not only illustrates the feasibility of the proposed velocimetric strategy in a relatively low speed range and in a rectilinear motion case but also implies a more important potential application. It is noted that the velocity of arterial blood flow in the human body is in the range of 40 to 100 cm/s,[27] that is, 1.44 to 3.6 km/h, which well matches the velocity range of above simulation. Therefore, the proposed velocimetry based on UPNCs is expected to be an alternative for the laser Doppler method applied in a blood flow monitor.[28]

In summary, this work proposed a speed sensing strategy based on upconversion spectral analysis, which utilizes the diversity in rising edges of the multiphoton process with different numbers of participated photons. Obviously, this strategy is appropriate for a large speed range with a quick response and high spatial resolution, enables the remote-type detection, and therefore is adoptable in vehicle monitoring, mechanical control, and medical diagnosis (in vivo blood flow monitoring). What is more, this strategy would exhibit somewhat superiority to conventional velocimetric methods. For example, compared with conventional spectral velocimetry, that is, the Doppler shift method, the proposed strategy allows a good separation between the excitation signal and detection signals, indicating a superior resolution. On the other hand, owing to the fast response, the velocity detected using our strategy is more close to the instantaneous linear speed, which would be more convenient than the reflection counting method and high-speed camera. Last but not the least, the proposed velocimetric mechanism in this work concerns the feature of the upconversion rising edge, which did not accept due attention before, and therefore would exploit novel issues in engineering and fabricating upconversion materials armed at sensing application.

METHODS

Numerical Simulation and Solving of the Rate Equations. According to the multi-energy-level model shown in Figure 1a, the populations of each energy level is noted as N_0, N_1, N_2., whose values follow the differential equations (eq 1). To solve these equations numerically, first, we assign the value of power (w) to be identically equal to 10 (steady-state excitation), the value of radiative transition rates of corresponding energy levels (A_1, A_2, A_3.) to be 100, and the absorption cross sections of each levels (C_0, C_1, C_2.) to be 1. Since we are only concerned with the relative intensity and time-related tendency, all these values are nondimensionalized. Then the Runge−Kutta iteration is carried out to solve the rate equations. The initial values are that, when $t = 0$, $N_0 = 1$ and $N_1 = N_2 = N_3 = N_4 = N_5 = 0$. Finally, all the obtained curves $N_x(t)$ are normalized to 1, as presented in Figure 1b.

In the case that pulse excitation is applied, the numerical solution of $N_x(t)$ ($x = 1, 2, 3.$) is divided into two sections: the pulse-on section and the pulse-off section. In the "on" section, the values of $N_x(t)$ are just the same as the case of steady-state excitation, while in the "off" section the value of power (w) is assigned to 0; therefore, the $N_x(t)$ is a simple decay curve ($\propto \exp(-A_x t)$), as shown in Figure 1c.

When simulating the case that the emitter is moving, we assign the size of the excitation beam spot (d) to be 1 (nondimensionalized value). The emitter is divided into several units whose sizes are equal to that of the excitation beam. Each unit is excited only when it passes through the region of the excitation beam spot and, therefore, is regarded as accepting only a pulse excitation (pulse width $\tau = d/v$, v is the moving speed). Hence, the overall luminescence behavior is approximated to continuous pulse emitting. Each pulse is calculated according to the above method. Herein, we assign the speed with three specific values ($v_1 = 2$, $v_2 = 3$, and $v_3 = 4$, nondimensionality).

Construction of the Speed-Controlled Turnplate. To construct a speed controllable turnplate, a motor with a rotating speed of 10500 rpm was employed. A 24 V DC voltage source was applied to drive the motor. Between the voltage source and the motor there equipped a function generator with a tunable duty ratio, which takes charge to control the rotating rate of the motor. A rounded cardboard with a diameter of 4.6 cm was fixed on the spindle of the motor forming a turnplate. The synthesized core−shell UCNCs were coated on the position of the cardboard with a diameter of 4.0 cm. The photograph of this setup is illustrated in Figure S4.

Velocimetry for an Object with Rectilinear Motion. A length-scaled air cushion track (1.5 m) was employed to carry out practical velocimetry for rectilinear motion. This track was tilted by 3° to enable the slide of a trolley with a length of 0.15 m on it. A 980 nm laser was used as the excitation whose light spot was fixed on the track. A CCD grating spectrograph (PR-670, Photo Research Inc.) was used to capture the temporal emission spectra from the trolley with an integral time of 500 ms. To obtain the rating curve, the initial positions of the trolley were chosen to be 1.0, 0.9, 0.8, 0.7, and 0.6 m away from the excitation laser spot so that, when it slides through the spot, the velocities would be different, specifically being 3.64, 3.45, 3.26, 3.05, and 2.82 km/h, respectively. For simulating velocimetry, the trolley was put on a random selected position (about 0.83 m away from the excitation spot) and was then let go to slide through the excitation spot.

ASSOCIATED CONTENT

Supporting Information

The Supporting Information is available free of charge at https://pubs.acs.org/doi/10.1021/acsami.9b17507.

Section S1−S3 describing establishment and analytical solutions of rate equations, synthesis of core−shell UCNCs, and characterizations. Figures S1−S8 showing FIR versus moving speed, XRD patterns, TEM and HRTEM images, photograph of the homemade speed-controlled turnplate, FIR versus speed fitted with quadratic polynomials, photo of the trolley, and background noise signal of the CCD spectrograph (PDF)

Movie showing the luminescence chromatic phenomenon of the UCNC-coated turnplate during an acceleration and deceleration cycle (AVI)

AUTHOR INFORMATION

Corresponding Authors

*E-mail: fengh@fjnu.edu.cn (F.H.).
*E-mail: dqchen@fjnu.edu.cn (D.C.).

ORCID

Yao Cheng: 0000-0003-1179-2886
Yuansheng Wang: 0000-0002-8117-2642
Daqin Chen: 0000-0003-0088-2480

Notes

The authors declare no competing financial interest.

ACKNOWLEDGMENTS

This work was supported by the National Natural Science Foundation of China (Grant Nos. 11574312, 51572065, 51972060) and the Fujian Provincial Orienting Sci & Tech Project (2018H0012).

REFERENCES

(1) Wang, F.; Liu, X. Recent Advances in the Chemistry of Lanthanide-Doped Upconversion Nanocrystals. *Chem. Soc. Rev.* **2009**, *38*, 976−989.

DOI: 10.1021/acsami.9b17507
ACS Appl. Mater. Interfaces XXXX, XXX, XXX−XXX

(2) Zheng, W.; Huang, P.; Tu, D.; Ma, E.; Zhu, H.; Chen, X. Lanthanide-doped Upconversion Nano-bioprobes: Electronic Structures, Optical Properties, and Biodetection. *Chem. Soc. Rev.* **2015**, *44*, 1379−1415.
(3) Lu, S.; Tu, D.; Hu, P.; Xu, J.; Li, R.; Wang, M.; Chen, Z.; Huang, M.; Chen, X. Multifunctional Nano-Bioprobes Based on Rattle-Structured Upconverting Luminescent Nanoparticles. *Angew. Chem., Int. Ed.* **2015**, *54*, 7915−7919.
(4) Amemori, S.; Sasaki, Y.; Yanai, N.; Kimizuka, N. Near-Infrared-to-Visible Photon Upconversion Sensitized by a Metal Complex with Spin-Forbidden yet Strong S0-T1 Absorption. *J. Am. Chem. Soc.* **2016**, *138*, 8702−8705.
(5) Eliseeva, S. V.; Bünzli, J. C. G. Lanthanide Luminescence for Functional Materials and Bio-Sciences. *Chem. Soc. Rev.* **2010**, *39*, 189−227.
(6) Zhu, X.; Su, Q.; Feng, W.; Li, F. Anti-Stokes Shift Luminescent Materials for Bio-Applications. *Chem. Soc. Rev.* **2017**, *46*, 1025−1039.
(7) Liu, Q.; Yin, B.; Yang, T.; Yang, Y.; Shen, Z.; Yao, P.; Li, F. A General Strategy for Biocompatible, High-Effective Upconversion Nanocapsules Based on Triplet-Triplet Annihilation. *J. Am. Chem. Soc.* **2013**, *135*, 5029−5037.
(8) Zhou, J.; Liu, Z.; Li, F. Upconversion Nanophosphors for Small-animal Imaging. *Chem. Soc. Rev.* **2012**, *41*, 1323−1349.
(9) Peng, H.; Stich, M. I. J.; Yu, J.; Sun, L.; Fischer, L. H.; Wolfbeis, O. S. Luminescent Europium(III) Nanoparticles for Sensing and Imaging of Temperature in the Physiological Range. *Adv. Mater.* **2010**, *22*, 716−719.
(10) Brites, C. D. S.; Lima, P. P.; Silva, N. J. O.; Millán, A.; Amaral, V. S.; Palacio, F.; Carlos, L. D. A Luminescent Molecular Thermometer for Long-Term Absolute Temperature Measurements at the Nanoscale. *Adv. Mater.* **2010**, *22*, 4499−4504.
(11) Gao, Y.; Huang, F.; Lin, H.; Zhou, J.; Xu, J.; Wang, Y. A Novel Optical Thermometry Strategy Based on Diverse Thermal Response from Two Intervalence Charge Transfer States. *Adv. Funct. Mater.* **2016**, *26*, 3139−3145.
(12) Cui, Y.; Yue, Y.; Qian, G.; Chen, B. Luminescent Functional Metal-Organic Frameworks. *Chem. Rev.* **2012**, *112*, 1126−1162.
(13) Hanaoka, K.; Kikuchi, K.; Kojima, H.; Urano, Y.; Nagano, T. Selective Detection of Zinc Ions with Novel Luminescent Lanthanide Probes. *Angew. Chem., Int. Ed.* **2003**, *42*, 2996−2999.
(14) Dong, H.; Sun, L.-D.; Yan, C.-H. Energy transfer in lanthanide upconversion studies for extended optical applications. *Chem. Soc. Rev.* **2015**, *44*, 1608−1634.
(15) Zhou, B.; Shi, B.; Jin, D.; Liu, X. Controlling Upconversion Nanocrystals for Emerging Applications. *Nat. Nanotechnol.* **2015**, *10*, 924−936.
(16) Hudry, D.; Howard, I. A.; Popescu, R.; Gerthsen, D.; Richards, B. S. *Adv. Mater.* **2019**, *31*, 1900623.
(17) Yang, D.; Ma, P.'a.; Hou, Z.; Cheng, Z.; Li, C.; Lin, J. Current Advances in Lanthanide Ion (Ln^{3+})-Based Upconversion Nanomaterials for Drug Delivery. *Chem. Soc. Rev.* **2015**, *44*, 1416−1448.
(18) Cheng, X.; Pan, Y.; Yuan, Z.; Wang, X.; Su, W.; Yin, L.; Xie, X.; Huang, L. Er^{3+} Sensitized Photon Upconversion Nanocrystals. *Adv. Funct. Mater.* **2018**, *28*, 1800208.
(19) Homann, C.; Krukewitt, L.; Frenzel, F.; Grauel, B.; Würth, C.; Resch-Genger, U.; Haase, M. $NaYF_4$:Yb,Er/$NaYF_4$ Core/Shell Nanocrystals with High Upconversion Luminescence Quantum Yield. *Angew. Chem., Int. Ed.* **2018**, *57*, 8765−8769.
(20) Zhou, B.; Yan, L.; Tao, L.; Song, N.; Wu, M.; Wang, T.; Zhang, Q. Enabling Photon Upconversion and Precise Control of Donor-Acceptor Interaction through Interfacial Energy Transfer. *Adv. Sci.* **2018**, *5*, 1700667.
(21) Deng, R.; Qin, F.; Chen, R.; Huang, W.; Hong, M.; Liu, X. Temporal Full-Colour Tuning Through Non-Steady-State Upconversion. *Nat. Nanotechnol.* **2015**, *10*, 237−242.
(22) Liu, H.; Huang, K.; Valiev, R. R.; Zhan, Q.; Zhang, Y.; Ågren, H. Photon Upconversion Kinetic Nanosystems and Their Optical Response. *Laser Photonics Rev.* **2018**, *12*, 1700144.
(23) Song, E.; Han, X.; Zhou, Y.; Wei, Y.; Jiang, X.-F.; Ye, S.; Zhou, B.; Xia, Z.; Zhang, Q. Long-lived Photon Upconversion Phosphorescence in $RbCaF_3$:Mn^{2+},Yb^{3+} and the Dynamic Color Separation Effect. *iScience* **2019**, *19*, 597−606.
(24) Xu, M.-m.; Sun, J.-f.; Zhang, B.; Zhang, G.; Lao, C.; He, H.-y.; Mao, A. Two-One-Way Laser Doppler Approach for Inter-Satellite Velocity Measurement. *Opt. Express* **2019**, *27*, 1353−1366.
(25) Hinsch, K. D. Holographic Particle Image Velocimetry. *Meas. Sci. Technol.* **2002**, *13*, R61−R72.
(26) Martin, M. J.; Brockett, S. W.; Selleck, R. R.; Croteau, G. M. Fiber-Optic Rotation Rate Sensor Having Dual Interferometer Loops. US Patent. US 4,639,138 A, 1987.
(27) Kashif, F. M.; Verghese, G. C.; Novak, V.; Czosnyka, M.; Heldt, T. Model-Based Noninvasive Estimation of Intracranial Pressure from Cerebral Blood Flow Velocity and Arterial Pressure. *Sci. Transl. Med.* **2012**, *4*, 129ra44.
(28) Riva, C. E.; Geiser, M.; Petrig, B. L.; Ocular Blood Flow Research Association. Ocular Blood Flow Assessment Using Continuous Laser Doppler Flowmetry. *Acta Ophthalmol.* **2010**, *88*, 622−629.

DOI: 10.1021/acsami.9b17507
ACS Appl. Mater. Interfaces XXXX, XXX, XXX−XXX